

Variations of the dust properties of M82 with galactocentric distance

Susan Hutton, Ignacio Ferreras^{*}, Vladimir Yershov

Mullard Space Science Laboratory, University College London, Holmbury St Mary, Dorking, Surrey RH5 6NT

Accepted for publication in MNRAS, 11 June 2015

ABSTRACT

We use near ultraviolet and optical photometry to investigate the dust properties in the nearby starburst galaxy M82. By combining imaging from the Swift/UVOT instrument and optical data from the Sloan Digital Sky Survey, we derive the extinction curve parameterized by the standard R_V factor, and the strength of the NUV 2175 Å feature – quantified by a parameter B – out to projected galactocentric distances of 4 kpc. Our analysis is robust against possible degeneracies from the properties of the underlying stellar populations. Both B and R_V correlate with galactocentric distance, revealing a systematic trend of the dust properties. Our results confirm previous findings that dust in M82 is better fit by a Milky Way standard extinction curve (Hutton et al.), in contrast to a Calzetti law. We find a strong correlation between R_V and B , towards a stronger NUV bump in regions with higher R_V , possibly reflecting a distribution with larger dust grain sizes. The data we use were taken before SN2014J, and therefore can be used to probe the properties of the interstellar medium before the event. Our R_V values around the position of the supernova are significantly higher than recent measurements post-SN2014J ($R_V \approx 1.4$). This result is consistent with a significant change in the dust properties after the supernova event, either from disruption of large grains or from the contribution by an intrinsic circumstellar component. Intrinsic variations among supernovae not accounted for could also give rise to this mismatch.

Key words: galaxies: individual: M82 – galaxies: starburst – galaxies: stellar content – galaxies: ISM – ISM: dust, extinction – supernovae: individual: SN 2014J

1 INTRODUCTION

Extinction in astronomy describes how much light is absorbed (or scattered) by dust grains in the medium between the source and the observer. Locally, extinction is measured by comparing the light emitted from stars of similar spectral type, for which differential variations from interstellar dust can be assessed. Local measurements in the Milky Way reveal a general trend in the extinction law although with significant scatter (see, e.g. Fitzpatrick & Massa 1990). The behaviour of the extinction law reveals the overall properties of the dust grains in the interstellar medium (Draine 2011). Closer to home, light scattered by the small air molecules in the atmosphere follow a typical $\propto \lambda^{-4}$ law that explains the blueness of the day-time sky. The typical Milky Way extinction law implies a shallower scaling dependence within the optical and near-infrared window, $\propto \lambda^{-1.5}$ (Cardelli et al. 1989; Fitzpatrick 1999). This

effective law results from the integration of the contribution from all grains in the dust component. A distribution with smaller grain sizes would make this law steeper, and a distribution with larger grains would induce a shallower dependence with wavelength, approaching the Mie regime (Draine 2011), where there is no wavelength dependence (i.e. clouds are white). One classical parameterisation of this smooth wavelength dependence is the ratio of total-to-selective extinction, $R_V \equiv A_V/E(B-V)$, where A_V is the extinction, measured in magnitudes, in the V band, and $E(B-V) = A_B - A_V$ is the colour excess, i.e. the additional reddening, measured as a $B-V$ colour, caused by dust. In addition to this smooth trend in the extinction law, there are some features characteristic of a specific component. In our analysis – extended to the near UV and optical spectral window – the most remarkable feature is the NUV bump at 2,175 Å (Stecher 1969), see Fig. 1. Although the component responsible for this feature is not confirmed, it is possibly carbonaceous material, graphite, or PAH molecules (Stecher & Donn 1965), although a more complex mixture is possible

^{*} E-mail: i.ferreras@ucl.ac.uk

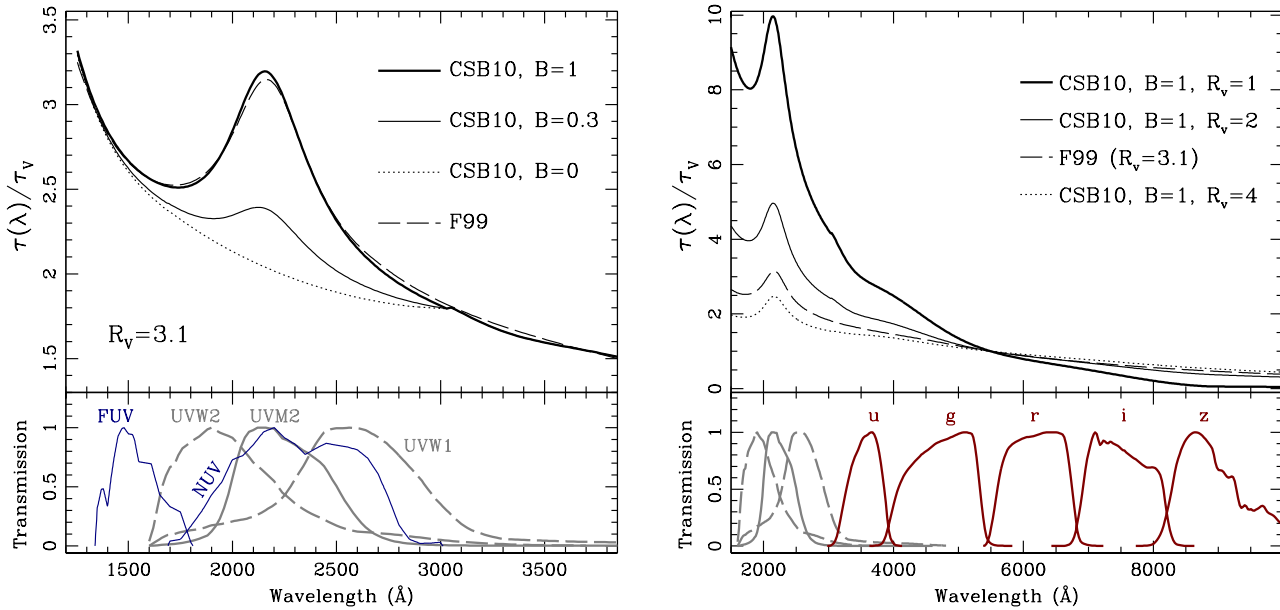


Figure 1. *Top:* Extinction law in the NUV (*left*) and NUV+optical (*right*) regions from Conroy et al. (2010, CSB10). Several cases of R_V and the NUV bump parameter B , are shown, as labelled. The CSB10 models on the left-hand panel all assume $R_V = 3.1$. In both figures, the dashed line shows for reference the Milky Way-standard extinction law (Fitzpatrick 1999, F99). *Bottom:* In grey we show the response functions of the NUV filters of Swift/UVOT (UVW2, UVM2 and UVW1). The passbands of GALEX (FUV and NUV) are also shown on the left-hand panel, and the filter response curves of SDSS (u, g, r, i, z) are shown in the right-hand panel. For each filter the effective throughput is divided by the peak transmission.

(Bradley et al. 2005). NUV observations of the Milky Way extinction curve consistently find this feature (see, e.g. Fitzpatrick & Massa 1986). In contrast, both lower metallicity regions, such as the Small Magellanic Cloud (Pei 1992), and starbursting galaxies (Calzetti 2001), lack the NUV bump.

An extinction law is a function that takes into account the wavelength-dependent obscuration due to absorption and scattering processes as light traverses a distribution of dust particles. One can therefore think of it as a foreground screen between the source and the observer. Such a scenario is a valid representation when observing stars in the Milky Way. However, when we extend the analysis of dust to distant, mostly unresolved, galaxies, this process is complicated by the distribution of the dust, the variation of the composition within the observed region, and the underlying stellar populations. It is common to refer to this integrated effect of dust in galaxies as attenuation. Galaxies with the same dust properties, hence with the same extinction, can yield different attenuation laws (see, e.g. Granato et al. 2000). For instance, the absence of the NUV bump in the attenuation law of starbursting galaxies (Calzetti 2001) can either be caused by an intrinsic lack of the component that causes this bump, or by the superposition of several stellar populations with different dust geometries (Panuzzo et al. 2007). Although it is beyond the scope of this paper to disentangle extinction and attenuation, one should bear in mind this subtlety in the interpretation of the observational constraints.

This work focuses on the dust component in the nearby starburst galaxy M82 (NGC 3034) located at a distance of ~ 3.3 - 3.5 Mpc (Dalcanton et al. 2009; Foley et al. 2014), with a dynamical mass of $\approx 10^{10} M_\odot$ (Greco, Martini & Thomp-

son 2012). The ongoing strong star formation in this galaxy is believed to have been triggered by a close encounter with the more massive galaxy M81, located in the same group. UV light extends out from the central regions of the galaxy where star formation is the strongest, revealing the presence of dust entrained in the supernovae-driven wind. In Hutton et al. (2014, hereafter HF14) we found that the dust obscuration in the NUV required the presence of an NUV bump, with the puzzling result that the prototypical starburst attenuation law of Calzetti (2001) — which features no NUV bump — gave poorer fits than the standard Milky Way extinction of Fitzpatrick (1999). This paper extends this issue by probing in more detail the dust properties of the interstellar medium (ISM) of M82, as a function of galactocentric distance.

Literally, as the accepted HF14 paper went to press, an enthusiastic and diligently-led team of students at UCL’s University of London observatory discovered SN2014J, a type Ia supernova, within 1 kpc of the central starburst of M82 (Fossey et al. 2014). A number of papers followed the evolution of the supernova (see, e.g., Goobar et al. 2014; Zheng et al. 2014), and, most relevant to this paper, the properties of the dust (see, e.g. Amanullah et al. 2014; Foley et al. 2014; Kawabata et al. 2014; Patat et al. 2014). We probe here the dust properties in the ISM of M82 pre-SN2014J, an issue of relevance to the understanding of the progenitor system of this supernova event.

The structure of the paper is as follows: the NUV-to-Optical data used for the analysis are presented in §2, followed by the modelling of the dust attenuation law in §3. The methodology followed to constrain the dust parameters

Table 1. Parameter range of the grid of simple stellar population models used to derive the effective dust-related properties.

Single Burst (1SSP): $\psi(t) \propto \delta(t - t_0)$			
Observable	Parameter	Range	Steps
Age	$\log(t_0/\text{Gyr})$	$[-2, +0.9]$	32
Metallicity	$\log Z/Z_\odot$	$[-1.5, +0.3]$	8
Total to selective extinction ratio	R_V	$[0.5, 4.5]$	32
NUV Bump strength	B	$[0, 1.3]$	32
Colour excess	E(B-V)	$[0, 1.5]$	32
Number of models		8,388,608	

via stellar population synthesis is explained in §4, with the results shown in §5, along with comparisons with the recent constraints on the dust properties from SN2014J. Finally, §6 closes with the conclusions of our analysis.

2 DATA

We use the same dataset as in HF14. In a nutshell, deep NUV images were retrieved from the HEASARC archive of *Swift*/UVOT. The Ultraviolet/Optical Telescope (UVOT, Roming et al. 2005) is a 30 cm instrument working as a photon counter, with three passbands in the NUV region, straddling the position of the 2,175Å bump. We refer the reader to Poole et al. (2008) and Breeveld et al. (2010) for details of the properties, mode of operation and data reduction procedure of UVOT imaging. We retrieved imaging data of M82 with total exposure times of 10.2, 13.9 and 8.7 ks in the UVW2, UVM2, and UVW1 passbands, respectively. The data were taken between 2008 and 2012, therefore our photometry corresponds to the galaxy before the SN2014J event. In addition to the UVOT data, we retrieved optical images from the SDSS DR8 server (Aihara et al. 2011). All images were registered to a common grid with a 0.5 arcsec pixel size (i.e. the UVOT reference). The optical (SDSS) images were convolved to a common spatial resolution with a Moffat profile. We note that the effective resolution of the UVOT images is $\sim 2.5 - 3$ arcsec. Photometry is performed within 5 arcsec (radius) apertures, following the standard calibration of the UVOT camera (Breeveld et al. 2010). The apertures were chosen to follow the disc of M82 (see fig. 2 of HF14). We also retrieved the GALEX/*FUV* images of M82 from the MAST archive, creating new sets of photometric measurements by convolving the UVOT data to the (poorer) resolution of GALEX¹ (~ 5 arcsec). Therefore, our combined dataset comprises photometry in the *FUV*, *UVW2*, *UVM2*, *UVW1*, *u*, *g*, *r*, *i*, *z* passbands. We refer the interested reader to HF14 for further details about the dataset.

There are, however, two differences with respect to the HF14 data. Here, we make use of an updated estimate of the foreground (Milky Way) reddening towards M82. In HF14 we took the value derived by Schlafly & Finkbeiner (2011), as given in the NED database, $E(B - V) = 0.140$ mag. Following the suggestion of Dalcanton et al. (2009), updated by Foley et al. (2014), we choose a lower estimate of 0.054 mag.

¹ Those lower resolution images were only used for the *FUV* – *UVW2* colour

This correction is due to the fact that M82 affects the reading of the large scale dust maps used for the determination of foreground reddening. This change affects the correction made to the observed photometry, and the derivation of the dust parameters, since in this paper, the amount of correction from the Milky Way – which follows a $R_V = 3.1$ Fitzpatrick (1999) law – is significantly reduced. Nevertheless, we find that our results are compatible with HF14. In addition, we use 3.3 Mpc for the distance to M82, for a more consistent comparison with recent papers (e.g. Foley et al. 2014). This change only affects the translation from angular distances to projected physical distances. The photometric apertures adopted in this paper map into a projected 160 pc diameter.

3 MODELLING THE ATTENUATION LAW

We follow the parameterisation of the attenuation law of Conroy et al. (2010, hereafter CSB10). This function depends on two basic parameters: R_V (defined in §1), and B , which controls the strength of the NUV bump. Fig. 1 shows a few realizations of the CSB10 function, along with the standard Milky Way attenuation law from Fitzpatrick (1999), assuming $R_V = 3.1$. Notice that within the NUV spectral window (left-hand panels), the UVOT filters sample the bump, with UVM2 located in the middle of the feature and UVW2/UVW1 straddling it on the blue and red sides, respectively. In addition, the GALEX/*FUV* filter includes an additional measurement blueward of the bump. The case $B=1$ corresponds very nearly to the standard Milky Way extinction curve, by construction. We follow a simple one-zone model for the dust component, assuming the light from the stellar populations is affected by a foreground dust screen. Other methods (e.g., Granato et al. 2000) would result in a more complex set of parameters, whereas we focus here on an “effective” attenuation law integrated to all the light within the aperture (see also Burgarella et al. 2005).

In HF14, we compared the NUV and optical photometry of M82 with a range of stellar population models, and two typical attenuation curves, the above mentioned Milky Way standard of Fitzpatrick (1999), and the law of Calzetti (2001) usually applied to star-bursting systems such as M82. We found that the latter – which lacks the presence of an NUV bump – gave poorer fits to the NUV photometry with respect to a Milky-Way law. In this paper, we explore in more detail this issue by use of the parameterization of CSB10.

In addition to the NUV bump, the photometric data

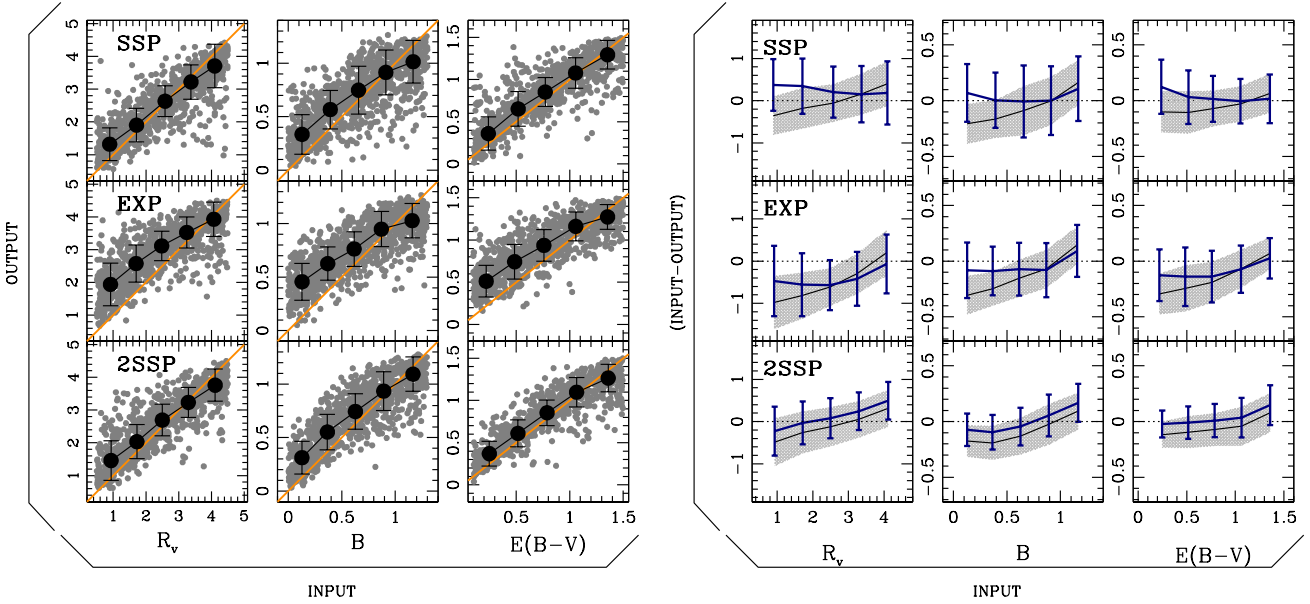


Figure 2. Results from simulated data. The same method used for the analysis of the NUV+optical photometry of M82 is applied to a set of simulated spectra. *Left:* Direct comparison between input (i.e. true) and output (i.e. retrieved) parameters. Each row represents a set of 1,000 simulations where the adopted star formation history is a simple stellar population (SSP, top); an exponentially decaying star formation rate (EXP, middle) or a two-burst history (2SSP, bottom). The grey dots are individual results, whereas the big circles and error bars are median and RMS values, binned at fixed number of data points per bin. *Right:* The comparison is given with respect to the difference between retrieved and true values, expressed as a fraction of the uncertainty. The grey shaded regions and lines are the raw results, whereas the blue error bars correspond to a correction based on a calibration of the output using these simulations (see Tab. 2 and text for details).

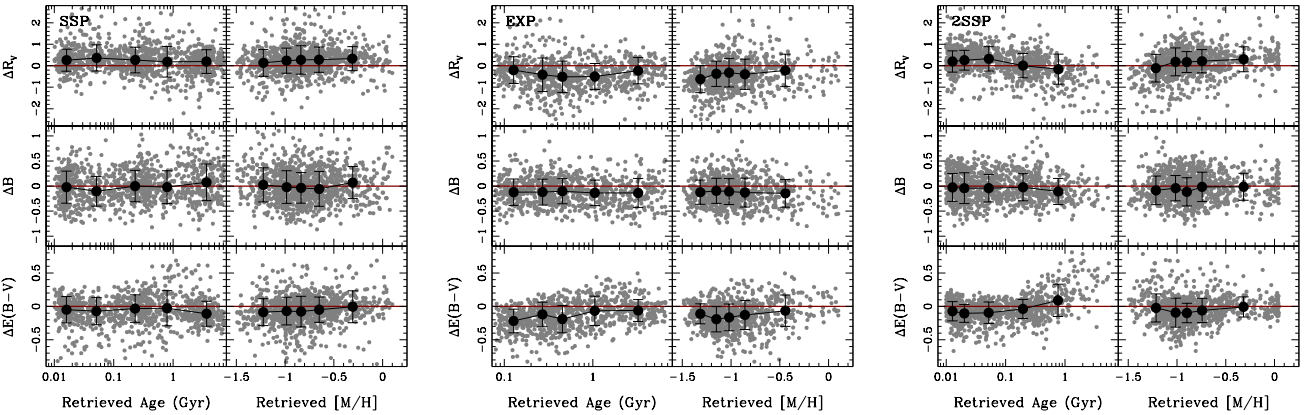


Figure 3. Trend of the retrieved dust parameters with the age and metallicity derived from the same likelihood function. The offset is defined as $\Delta\pi \equiv \pi(\text{in}) - \pi(\text{out})$, where π represents any of the three dust-related parameters. There is no significant bias in the dust parameters with respect to the underlying stellar populations.

can be used to constrain the parameter R_V , which depends on the composition of the dust grains. A standard Milky Way law assumes $R_V = 3.1$, although with significant scatter, roughly between 2.2 and 5.8 (Fitzpatrick 1999). Lower (higher) values of R_V will require a distribution of smaller (larger) dust grains, with respect to the Milky Way standard. In HF14, we studied the extraplanar light originated from the reflection of the stellar light in the galaxy, that

impinged on the dust grains above and below the galactic plane. These dust grains were entrained in the material ejected by the strong galactic winds triggered by the starburst. We fitted the photometric data assuming the absorption/scattering processes are described by a power law ($\propto \lambda^{-x}$), finding a value ($x = 1.53 \pm 0.17$). Note, however, that this case pertains to the scattering of light from dust grains in the extraplanar wind region, as they are illumi-

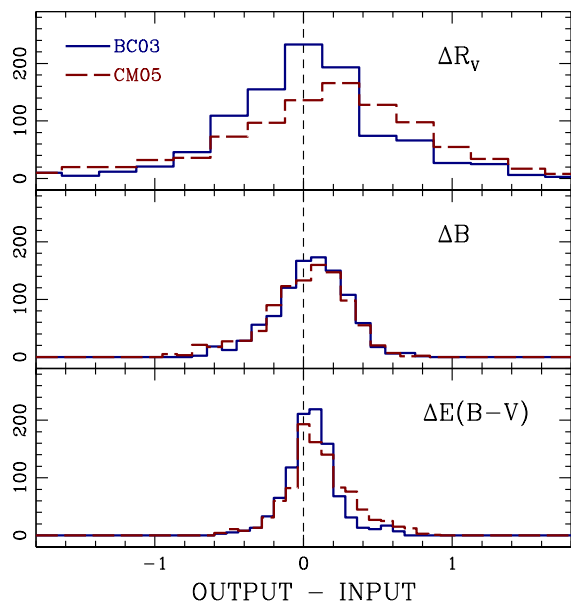


Figure 4. Histogram comparing the difference between the “true” (input) and the retrieved (output) dust-related parameters, for two choices of population synthesis models. The methodology is the same in both cases, using a grid of SSP models from Bruzual & Charlot (2003). The blue solid histograms show the parameter retrieval accuracy when using a range of simulations constructed from Bruzual & Charlot (2003) models. The red dashed histograms correspond to simulations assembled from the models of Maraston (2005). No significant bias is found (see text for details).

nated by the galaxy. In contrast, we focus in this paper on the effective attenuation law in the main body of the galaxy.

The right-hand panels of Fig. 1 show a wide NUV/optical spectral window, focusing on variations of R_V . Note how higher values of R_V – as expected in an ISM with larger dust grains – result in a flatter attenuation law, closer to the Mie regime. Therefore, the use of a wide spectral range (NUV and optical photometry) will allow us to constrain this parameter.

4 CONSTRAINING THE DUST VALUES

In order to constrain the dust attenuation parameters, we need to quantify the effect of the other, “nuisance”, parameters related to the underlying stellar population. Our methodology involves a comparison of the observed NUV and optical photometry with a large grid of synthetic populations from the models of Bruzual & Charlot (2003). Tab. 1 shows the grid of 8,388,608 models used in this paper. They correspond to simple stellar populations (SSP, representing a population with a single age and metallicity) for a standard initial mass function (Chabrier 2003). Within our wavelength interval, dust simply introduces a smooth, long (spectral) range behaviour (aside from the NUV bump). Therefore it is possible to factor out the attenuation law from the different trends introduced in the photometry by the age and metallicity distribution of the populations. To prove this

point, we ran three sets of simulations, each one with a different assumption about the star formation history: i) SSP (as above); ii) EXP: a composite of stellar populations following an exponentially decaying star formation rate, choosing the formation epoch, decay timescale and metallicity as free parameters of the populations; iii) 2SSP, a superposition of two SSPs, where the age of the young and old components, the fractional contribution, by mass, of the young component, and the metallicity are free parameters. These three choices encompass a wide range of both smooth and bursty star formation histories. This exercise serves to understand whether systematic biases are being introduced because of a methodology where the analysis is based on a grid of SSPs.

The derivation of the model parameters follows a Bayesian approach, using a χ^2 -based likelihood as a probability distribution function ($\mathcal{L} \propto e^{-\Delta\chi^2/2}$) from which we derive the errors as the 68% confidence level of this distribution. $\Delta\chi^2$ is defined as $\chi^2 - \chi^2_{\min}$, and χ^2 is given by:

$$\chi^2(\pi_i) \equiv \sum_j \frac{[m_j^{\text{OBS}} - m_j^{\text{MODEL}}(\pi_i)]^2}{\sigma^2(m_j)},$$

where $\{\pi_i\}$ represents all possible choices of the five parameters listed in Tab. 1. m_j^{OBS} and m_j^{MODEL} are the observed and model magnitudes, respectively, as follows: $\{FUV, UVW2, UVM2, UVW1, u, g, r, i, z\}$. Finally, $\sigma(m_j)$ is the observational errors for each magnitude. In addition to the parameters listed in Tab. 1, we include a “normalization” parameter that assumes the model SDSS g band magnitude lies somewhere between $g_{\text{OBS}} \pm 0.1$ mag; where g_{OBS} is the observed magnitude in the g band for each aperture. The extracted parameters are then computed using the likelihood as a probability distribution function, namely:

$$\langle \pi_i \rangle = \frac{\int d\pi_1 \cdots d\pi_5 \mathcal{L}(\pi) \pi_i}{\int d\pi_1 \cdots d\pi_5 \mathcal{L}(\pi)} \quad (1)$$

The priors applied in the analysis are simply the range of parameters explored, as shown in Tab. 1 (i.e. one can consider them as “flat priors”, giving equal probability within the range stated).

Fig. 2 shows the results for $3 \times 1,000$ simulations corresponding to each of the three formation histories. The simulated data explore a wide range of ages, metallicities, and dust properties, comparable to those found in M82 (see fig. 5 of HF14). Our analysis marginalizes over the stellar population properties, and produces the extinction-related constraints on – from left to right – R_V , B and $E(B-V)$. The first two parameters are intrinsic to the effective dust attenuation law, whereas the latter can be considered as a normalization factor, reflecting the amount of dust present. The panels on the left compare input value (abscissa) versus retrieved value (ordinate). An orange line in each panel gives the 1:1 correspondence. The grey dots are results from individual estimates, whereas the black dots and error bars mark the median and root-mean square values, respectively, when binned at fixed number of data points per bin. Note that no large bias is obtained, regardless of the use of different star formation histories (top to bottom). The derivation of the NUV bump strength only uses the UV photometry for the definition of the likelihood, since the optical photometry is fully insensitive to the presence of this bump (Fig. 1 right-hand panel), and would therefore “wash-out” the constraining power in the comparison.

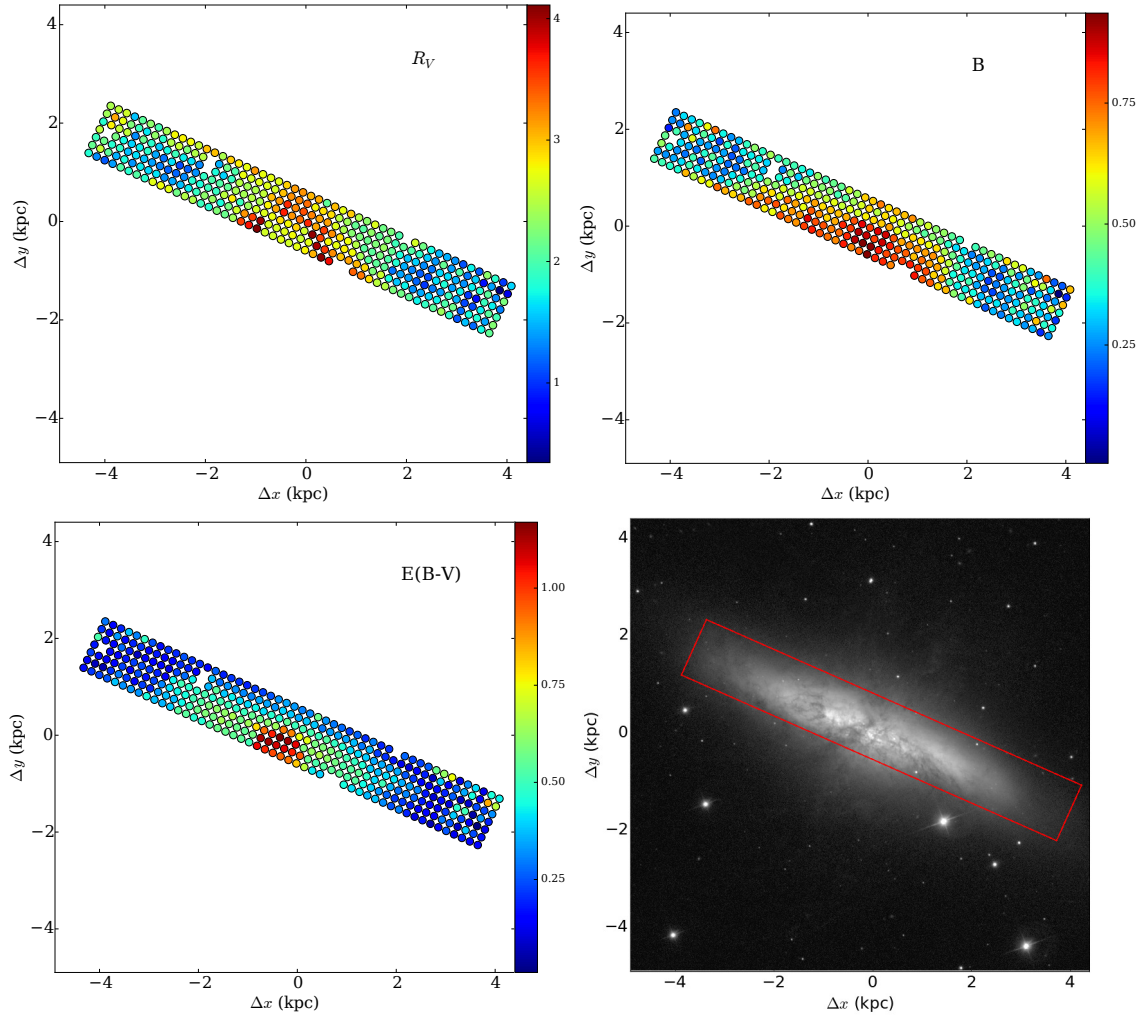


Figure 5. Two-dimensional distribution of the retrieved values of the parameters that define the dust attenuation law used in this paper (see text for details). The ratio of total-to-selective attenuation (*top-left*), NUV bump strength (*top-right*) and colour excess (*bottom-left*) are shown as a colour-coded map, with the contiguous colour bars showing the mapping in each panel. The x-y coordinates are given as physical projected distances in kpc. The bottom-right panel shows a *g*-band image from SDSS-DR10 at the same scale.

We use the comparison with the simulated data to derive a mean linear correction between input and output parameters. The results of the fits are shown in Tab. 2. Since one cannot determine the best star formation history corresponding to the real data, we decided to choose for the general correction the one that gave the best compromise among the three sets of star formation histories, i.e. we used the results from all three sets of simulations for the fit. The right-hand panels of Fig. 2 illustrate the validity of this correction and the retrieved error bars. They compare the difference between the “true” and the extracted value (“input” – “output” in the figure). This comparison allows us to determine whether the quoted error bars are valid. The shaded regions correspond to the original data, whereas the blue lines with error bars give the results for the corrected parameters. Note that the corrections are relatively minor with respect to the error bar, and no significant bias is apparent when the corrections are taken into account. Nevertheless, we will show in the next figures our results with and without this correction. The comparison with simulated

data therefore confirms that it is possible to factor out the attenuation law from the properties of the underlying, unresolved stellar populations, by use of a large library of simple stellar populations.

We also need to assess a possible bias between the dust related parameters ($R_V, B, E(B - V)$) and the underlying stellar populations. In Fig. 3 we compare the bias $\Delta\pi \equiv \pi(\text{in}) - \pi(\text{out})$ – where π represents any of the three dust-related parameters – as a function of the retrieved age and metallicity. Note that the input parameters are, by construction, uncorrelated. The figure shows that most of the comparisons give negligible dependence on age and metallicity, or on the functional form of the star formation history. This result is very important for the interpretation of the radial gradients of the effective attenuation law presented in the next section. We also note that the values we retrieve for the SSP ages are consistent with Hutton et al. (2014), where only two standard extinction laws were considered. These results are also consistent with independent estimates, giving ages around 0.4–1 Gyr within the central 3 kpc, with older

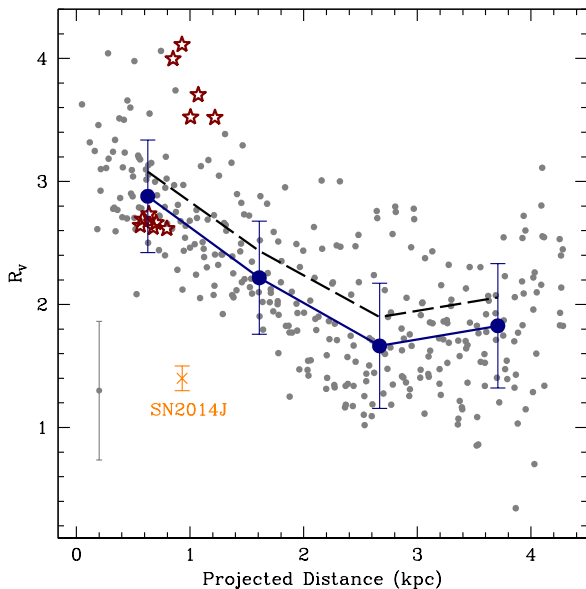


Figure 6. Retrieved values for the ratio of total-to-selective extinction R_V as a function of projected galactocentric distance. The grey dots represent individual measurements, with a characteristic error bar shown on the left-hand side of the figure. The red stars are measurements within 30 arcsec (i.e. 480 pc) of the position of SN2014J. The blue dots and error bars are the median and root mean square values of the data, binned at a fixed number of data points per bin. The black line shows the same result if the retrieved parameters are not calibrated with respect to the simulations (see Tab. 2). The orange cross and error bar correspond to the measurement in the region of SN2014J after the event (Amanullah et al. 2014)

ages in the outer regions; and a colour excess $E(B-V) \sim 0.4$ with a significant increase in the central regions (see, e.g. Mayya et al. 2006; Rodríguez-Merino et al. 2011). As regards to metallicity, we emphasize that broadband photometric analyses have large degeneracies with respect to this parameter. Our simulations in fact show that of all five parameters given in Tab. 1, metallicity is the only one that fails at retrieving the input values, within a 0.5 dex uncertainty. However, we emphasize that such a result does not prevent us from deriving unbiased estimates of the other parameters (see Fig. 2), and consider age and metallicity simply as nuisance parameters in the derivation of the dust-related properties. In addition, we have done tests, imposing the typical metallicities expected in M82 (e.g. Origlia et al. 2004) as priors, and the extracted values of R_V , B , and $E(B-V)$ are unaffected. A partial version of the parameters derived from this analysis are shown in Tab. 3. The complete version can be retrieved online.

Finally, in order to assess the possible systematics caused by the specific population synthesis model used, we create an additional set of 1,000 simulations with the models of Maraston (2005). We note that these models apply widely different prescriptions, including a different treatment of the thermally-pulsing AGB phase, which can be prominent in populations of ages ~ 1 Gyr, therefore relevant for the study of M82. We emphasize here that the aim in this paper is *not*

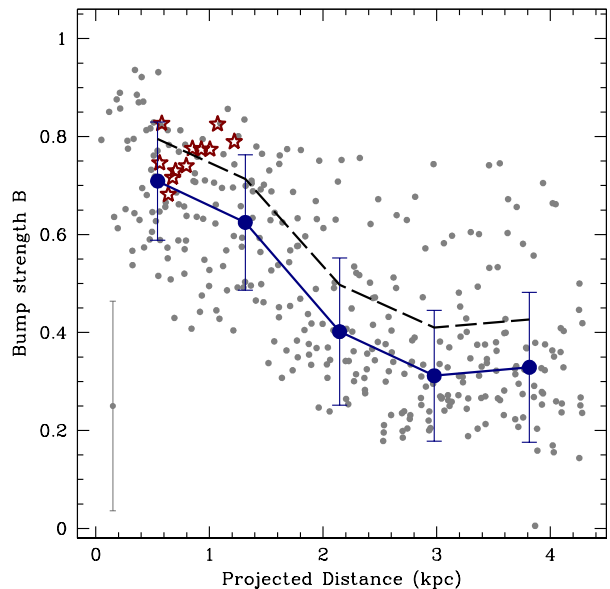


Figure 7. The observational constraints on the NUV bump strength, B , are plotted with respect to the projected galactocentric distance. The symbols are the same as in Fig. 6.

to constrain the age or metallicity composition of the populations, but to factor out the degeneracies caused by these parameters. In order to show that our results are robust against different prescriptions for the population synthesis models, we treat the simulated data – which use the Maraston (2005) – models, with the same grid of SSPs – which are based on the Bruzual & Charlot (2003) models. Fig. 4 shows the histograms of the difference between the “true” (i.e. the assumed value) parameter, and the retrieved one, in both cases (BC03: for the simulated data based on Bruzual & Charlot (2003) models; CM05 for the data based on the Maraston (2005) models). We conclude that our derivation of the dust-related parameters is robust.

5 THE ATTENUATION LAW OF M82

Fig. 5 shows the spatial distribution of the dust-related parameters constrained with the photometry. The results are shown as colour-maps. The missing apertures in the distribution are masked out because of the presence of foreground stars. The bottom-right panel includes an SDSS- g band image of the galaxy, shown at the same scale. The radial profile of the constraints on the dust properties of M82 are shown in Fig. 6 (R_V); Fig. 7 (NUV bump strength); and Fig. 8 (colour excess). In all figures the grey dots correspond to individual measurements, with a typical error bar shown on the left-hand side. The median and root-mean-square values of the data, binned at fixed number of data points per bin, are shown as black solid dots with error bars. Finally, the solid line without error bars show the result if the calibration – presented in Tab. 2 – is not applied. Note the significant trend with galacto-centric distance. The central region of M82 – which due to projection effects include *both*

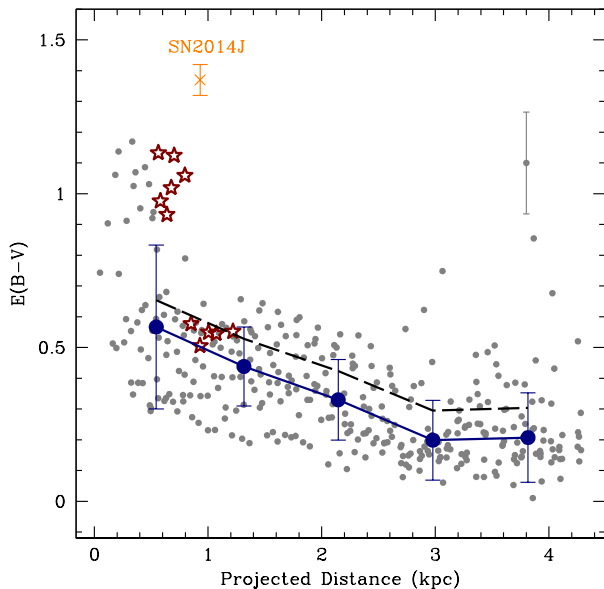


Figure 8. The best fits to the colour excess, $E(B-V)$, are shown against galactocentric distance. The symbols are the same as in Fig. 6.

the starbursting region and the outer areas – has a more standard attenuation law, compatible with the $R_V=3.1$ and $B=1$ values corresponding to the Fitzpatrick (1999) case. As we probe further out, the total-to-selective extinction ratio parameter, R_V , decreases, and so does the NUV bump strength, although we never find measurements compatible with a weak or non-existent bump. The colour excess also depends on galacto-centric distance, although in this case the correlation is more tightly linked to the variation in the metallicity and star formation distribution.

We note that this result is robust against a possible bias caused by the inherent radial trend in age and metallicity found in galaxies. The previous section explored through simulations the possibility of a bias in the derivation of the parameters related to the dust composition, to find no significant systematic trends with age, metallicity or the different functional form of the star formation history. Therefore, these trends are intrinsic radial variations of the effective dust attenuation law (R_V, B), and the amount of dust ($E(B-V)$).

Fig. 9 shows the correlations among the three dust-related parameters (using the same symbols as in the previous figures). The range of values found *within* M82 is comparable with the average estimates of Conroy et al. (2010) for a general sample of galaxies ($R_V=2.0$; $B=0.8$). Our values are also consistent with the sample of nearby galaxies of Burgarella et al. (2005), who find a range of values for the NUV bump strength, weaker than Milky Way standard, in the range² $B\sim 0.5-0.6$. Note the significant trend between R_V and B (top-left panel of Fig. 9), suggestive of a strong

² We translate their A_{bump} to the B parameterisation of Conroy et al. (2010) by a simple comparison of the effective attenuation laws.

Table 2. Corrections to the data, derived from simulations (see §4). Col. 1 gives the parameter (π), cols. 2 and 3 are the slope and intercept of the correction; col.4 gives the scatter with respect to the full set of $3\times 1,000$ simulated data points (given as RMS); col. 5 is the bias, i.e. the offset between the fit and the data points.

$\pi_{\text{TRUE}} = \alpha\pi_{\text{OBS}} + \beta$			
π	α	β	RMS
R_V	1.030203	-0.292036	0.625
B	1.032269	-0.111693	0.225
$E(B-V)$	1.027146	-0.104647	0.194

link between the overall dust grain size distribution (larger grains causing higher values of R_V) and the carrier of the NUV bump strength. Although changes in the attenuation law can be produced by changes in the age-dependent extinction of the geometry of the stellar/dust components, our study – based on a single galaxy – would suggest that most of the variations are caused by the intrinsic extinction law. A similar trend is found between B and colour reddening, although in this case the data mostly show that regions with high reddening ($E(B-V) > 0.5$) have high NUV bump strengths (whereas less dusty regions can have a wide range of B , including $B=1$). In a similar way, regions with high reddening are associated with higher values of R_V (top-right panel), corresponding to the presence of larger dust grains.

5.1 The ISM around SN2014J in the pre-supernova phase

Our data are especially relevant to explore the region around the recent SN2014J event. We use the position of the supernova from Tendulkar et al. (2014) to locate the relevant apertures in our dataset. In Fig. 6, 7, 8, we show with red star symbols the estimates of $R_V, B, E(B-V)$, respectively, measured in the apertures located within 30 arcsec of the SN2014J event, corresponding to a projected distance of 480 pc. Notice that those regions feature higher values of R_V ($\sim 3-4$) than the recent estimates determined post-SN2014J ($R_V = 1.4 \pm 0.1$, Amanullah et al. 2014, orange cross). In general, photometric studies of the environment of type Ia supernova favour low values of R_V (Burns et al. 2014), however the dispersion is quite large (Amanullah et al. 2015). For this particular case, even within the error bars and the dispersion of the data, it is not possible to assume that post-SN2014J the dust properties in this region are compatible. Therefore, our results indicate that pre-SN2014J, this region had a dust content in the ISM similar to the Milky Way standard. Such a result implies the post-SN2014J observations should be explained either by a combination both from dust in the ISM surrounding the supernova and the intrinsic contribution from a circumstellar disk (Foley et al. 2014, although see Phillips et al. 2013), or by a significant change in the ISM towards the observed region. Alternatively, one could also expect that supernovae have intrinsic variations in colour that are not accounted for, or that the distribution of dust within the line of sight towards the supernova can produce the mismatch.

Table 3. Dust-related parameters and SSP ages derived from the analysis. Cols. 1 and 2 give the celestial coordinates of the central position of each aperture. Col. 3 is the corresponding projected galactocentric distance. Col. 4 is the total-to-selective attenuation ratio. Col. 5 is the NUV bump strength. Col. 6 is the colour excess, and col. 7 gives the base-10 logarithm of the SSP age, expressed in Gyr. Uncertainties are quoted at the 1σ level.

RA	Dec.	ΔR	R_V	B	$E(B-V)$	log Age
J2000		kpc				Gyr
⋮	⋮	⋮	⋮	⋮	⋮	⋮
148.95876	69.67534	0.365	2.594 ± 0.089	0.936 ± 0.128	1.025 ± 0.042	-1.979 ± 0.060
148.95539	69.67785	0.195	2.612 ± 0.095	0.876 ± 0.135	1.061 ± 0.048	-1.921 ± 0.153
148.95203	69.68039	0.053	3.626 ± 0.657	0.793 ± 0.147	0.743 ± 0.188	-0.554 ± 0.710
148.94867	69.68293	0.171	3.247 ± 0.570	0.636 ± 0.161	0.513 ± 0.186	-0.147 ± 0.603
148.94530	69.68547	0.344	2.777 ± 0.676	0.537 ± 0.150	0.386 ± 0.208	-0.133 ± 0.703
⋮	⋮	⋮	⋮	⋮	⋮	⋮

This is an excerpt from the central region. The full version of this table can be retrieved online.

5.2 Are the dust properties of M82 different from other galaxies?

We note that the trends presented in this paper are at odds with some recent results targeting our galaxy and M31. In Nataf et al. (2013) and Nishiyama et al. (2009), the dust attenuation properties of the Milky Way are probed towards the Galactic bulge, finding a steeper law – i.e. lower R_V . In addition, Dong et al. (2014) find similar trends in the Andromeda Galaxy. We note that the populations towards the centre of M82 are significantly different from these two galaxies. The presence of a strong starburst will affect the properties of the ISM, and the dust. In addition, the nearly edge-on orientation of M82 along with its dusty ISM results in a complex interpretation of the results towards small *projected* galactocentric radii.

Another interesting issue is the strong correlation between R_V and bump strength (top-left panel of Fig. 9). A recent study of the NUV bump strength in high redshift galaxies (Kriek & Conroy 2013) suggests the opposite trend, namely a *decreasing* bump strength with increasing R_V . In contrast, detailed studies in our Galaxy do not seem to find a correlation (Fitzpatrick & Massa 2007), so there is still no clear indication whether such a correlation should be expected in general.

We emphasize here that our methodology is unlikely to produce a spurious correlation between these two parameters. The simulations show that the (uncorrelated) dust parameters are retrieved without any significant bias or artificial correlation among parameters. In addition, we note that our study mainly differs from Kriek & Conroy (2013) in the sense that we explore *internal* variations within the same galaxy, rather than trends among galaxies.

6 CONCLUSIONS

We revisit the NUV and optical photometry of M82, presented in HF14, to constrain in more detail the properties of the dust attenuation law. Through the analysis of simulated data, we prove that it is possible to factor out the contribution from the underlying stellar populations, setting constraints on the NUV bump strength and the total-

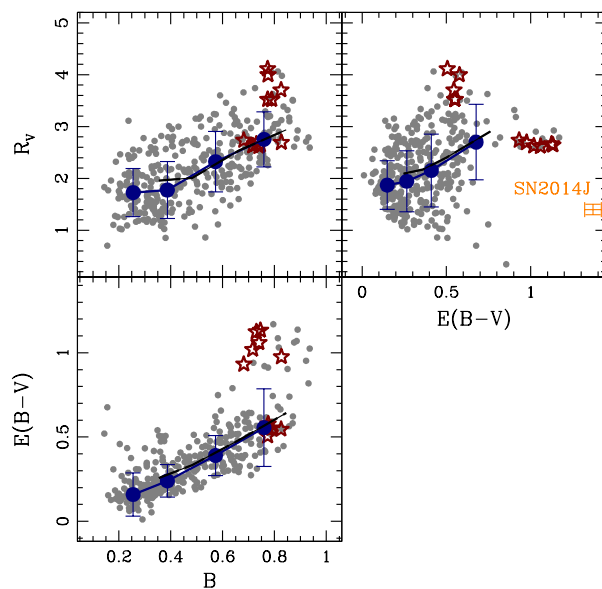


Figure 9. Correlations among the fitted dust-related parameters. The symbols are the same as in Fig. 6.

to-selective attenuation ratio R_V . We find a significant gradient with projected galactocentric distance (Fig. 6), with the central regions showing a standard Milky Way attenuation law, progressing outwards towards an extinction with a weaker NUV bump and steeper R_V , more characteristic of a smaller grain size distribution, effectively tending towards the standard attenuation law of the SMC (Pei 1992). We should note here that our results correspond to a one-zone model, where the dust only contributes as a foreground screen. Changes in the geometry of the dust distribution can therefore cause variations on the dust parameters presented here (see, e.g., Witt & Gordon 2000).

As regards to the NUV bump strength, we find a systematic decrease outwards. The weaker bump in the outer regions can be indicative of changes in the dust properties (Gordon, Calzetti, & Witt 1997), although an age-dependent

attenuation law can produce similar effects (Panuzzo et al. 2007). However, our observational constraints go in the opposite way with respect to the models. A trend towards a weaker bump is found at large galacto-centric distances, away from the central starburst, where the dust content is lower, and where R_V is low, indicative of smaller dust grains (see Fig. 9). Our results confirm HF14 in the sense that a Milky Way law, with a significant NUV bump is favoured with respect to a Calzetti (2001) law, in the central starburst.

Our work is most relevant to the analysis of the environment of the recent type Ia supernova SN2014J. Our data were taken before the event, and therefore probe the properties of the dust of the ISM. At the position of SN2014J, we find a standard dust component, typical of the Milky Way, with $R_V \sim 3$ and $B \sim 1$. Therefore, the recent measurements with lower values of R_V reflect either the presence of a circumstellar component, or a significant change in the dust properties within the volume probed by the post-SN2014J measurements.

ACKNOWLEDGEMENTS

We would like to thank the anonymous referee for very valuable comments and suggestions. This research has made use of data and software provided by the High Energy Astrophysics Science Archive Research Center (HEASARC), which is a service of the Astrophysics Science Division at NASA/GSFC and the High Energy Astrophysics Division of the Smithsonian Astrophysical Observatory. We acknowledge use of imaging data from the Sloan Digital Sky Survey (SDSS). Funding for SDSS-III has been provided by the Alfred P. Sloan Foundation, the Participating Institutions, the National Science Foundation, and the U.S. Department of Energy Office of Science. The SDSS-III web site is <http://www.sdss3.org/>. We also thank the Mikulski Archive for Space Telescopes (MAST). STScI is operated by the Association of Universities for Research in Astronomy, Inc., under NASA contract NAS5-26555. Support for MAST for non-HST data is provided by the NASA Office of Space Science via grant NNX13AC07G and by other grants and contracts.

REFERENCES

- Amanullah, R., et al., 2015, arXiv:1504.02101
Amanullah, R., et al., 2014, ApJ, 788, 21
Aihara, H., et al. 2011, ApJS, 193, 29
Bradley, J., et al., 2005, Sci, 307, 244
Breeveld, A. A., et al., 2010, MNRAS, 406, 1687
Bruzual, G. & Charlot, S., 2003, MNRAS, 344, 1000
Burgarella, D., Buat, V., Iglesias-Páramo, J., 2005, MNRAS, 360, 1413
Burns, C. R., et al., 2014, ApJ, 789, 32
Calzetti, D., 2001, New Ast., 45, 601
Cardelli J. A., Clayton G. C., Mathis J. S., 1989, ApJ, 345, 245
Chabrier, G., 2003, PASP, 115, 763
Conroy, C., Schiminovich, D., Blanton, M. R., 2010, ApJ, 718, 184
Dalcanton, J. J., et al., 2009, ApJS, 183, 67
Dong, H., et al. 2014, ApJ, 785, 136
Draine B. T., 2011, Physics of the Interstellar and Inter-galactic Medium. Princeton Univ. Press, Princeton, NJ
Fitzpatrick E. L., Massa D., 1986, ApJ, 307, 286
Fitzpatrick E. L., Massa D. L., 1990, ApJS, 72, 163
Fitzpatrick E. L., Massa D. L., 2007, ApJ, 663, 320
Fitzpatrick, E. L., 1999, PASP, 111, 63
Foley, R. J., et al. 2014, MNRAS, 443, 2887
Fossey J., Cooke B., Pollack G., Wilde M., Wright T., 2014, Central Bureau Electronic Telegrams, 3792, 1
Gordon K. D., Calzetti D., Witt A. N., 1997, ApJ, 487, 625
Granato, G. L., Lacey, C. G., Silva, L., Bressan, A., Baugh, C. M., Cole, S., Frenk, C. S., 2000, ApJ, 542, 710
Goobar, A., et al., 2014, ApJ, 784, L12
Greco, J. P., Martini, P., Thompson, T. A., 2012, ApJ, 757, 24
Hutton, S., et al., Ferreras, I., Wu, K., Kuin, P., Breeveld, A., Yershov, V., Cropper, M., Page, M., 2014, MNRAS, 440, 150
Kawabata, K. S., et al. 2014, ApJ, 795, L4
Kriek, M., Conroy, C., 2013, ApJ, 775, L16
Maraston, C., 2005, MNRAS, 362, 799
Mayya, Y. D., Bressan, A., Carrasco, L., Hernández-Martínez, L., 2006, ApJ, 649, 172
Nataf, D. M., et al., 2013, ApJ, 769, 88
Nishiyama, S., Tamura, M., Hatano, H., Kato, D., Tanabé, T., Sugitani, K., Nagata, T., 2009, ApJ, 696, 1407
Origlia, L., Ranalli, P., Comastri, A., Maiolino, R., 2004, ApJ, 606, 862
Panuzzo, P., Granato, G. L., Buat, V., Inoue, A. K., Silva, L., Iglesias-Páramo, J., Bressan, A., 2007, MNRAS, 375, 640
Patat, F., et al., 2014, arXiv:1407.0136
Pei, Y C., 1992, ApJ, 395, 130
Phillips, M. M., et al., 2013, ApJ, 779, 38
Poole, T. S., et al., 2008, MNRAS, 383, 627
Rodríguez-Merino, L. H., Rosa-González, D., Mayya, Y. D., 2011, ApJ, 726, 51
Romig, P. W. A., et al., 2005, Space Sci. Rev., 120, 95
Schaflly, E. F., Finkbeiner, D. P., 2011, ApJ, 737, 103
Stecher, T. P. Donn, B., 1965, ApJ, 142, 1681
Stecher, T. P., 1969, ApJ, 157, L125
Tendulkar, S. P., et al. 2014, A.Tel., 5789, 1
Witt, A. N., Gordon, K. D., 2000, ApJ, 528, 799
Zheng, W., et al. 2014, ApJ, 783, L24